Surface rupture and shallow fault reactivation during the 2019 Mw 4.9 Le Teil earthquake, France

Jean-François Ritz, Stéphane Baize, Matthieu Ferry, Christophe Larroque, Laurence Audin, Bertrand Delouis, Emmanuel Mathot

COMMUNICATIONS EARTH&ENVIRONMENT

ARTICLE

https://doi.org/10.1038/s43247-020-0012-z OPEN

Surface rupture and shallow fault reactivation during the 2019 Mw 4.9 Le Teil earthquake, France

Jean-François Ritz[1✉], Stéphane Baize[2], Matthieu Ferry[1], Christophe Larroque[3], Laurence Audin[4], Bertrand Delouis[3] & Emmanuel Mathot[5]

The Rhône River Valley in France, a densely populated area with many industrial facilities including several nuclear power plants, was shaken on November 11th 2019, by the Mw 4.9 Le Teil earthquake. Here, we report field, seismological and interferometric synthetic-aperture radar observations indicating that the earthquake occurred at a very shallow focal depth on a southeast-dipping reverse-fault. We show evidence of surface rupture and up to 15 cm uplift of the hanging wall along a northeast-southwest trending discontinuity with a length of about 5 km. Together, these lines of evidence suggest that the Oligocene La Rouvière fault was reactivated. Based on the absence of geomorphic evidence of cumulative compressional deformation along the fault, we suggest that it had not ruptured for several thousand or even tens of thousands of years. Our observations raise the question of whether displacement from surface rupture represents a hazard in regions with strong tectonic inheritance and very low strain rates.

[1] Géosciences Montpellier, Univ. Montpellier, CNRS, Univ. Antilles, Montpellier, France. [2] IRSN, Institute of Radiological Protection and Nuclear Safety, Fontenay-aux-roses, France. [3] Géoazur, Univ. Côte d'Azur, CNRS, Observatoire de la Côte d'Azur, IRD, Valbonne, France. [4] ISTerre, Univ. Grenoble Alpes, CNRS, IRD, Grenoble, France. [5] Terradue Srl, Rome, Italy. ✉email: jean-francois.ritz@gm.univ-montp2.fr

On 11 November 2019, a M_w 4.9 surface-rupturing earthquake occurred in Le Teil, near the city of Montélimar within the Rhône River Valley, a densely populated area in southern France with numerous industrial facilities, including several nuclear power plants. The earthquake caused significant damages (epicentral intensity VII to VIII EMS98) in the villages of Le Teil, Saint-Thomé, and Viviers, fissuring thick walls and falling roof tiles, chimneys, and window frames from houses. Locally, the first two villages were especially affected with the partial collapse of several cobble stone masonry buildings. In total, more than 900 houses and buildings have been seriously damaged in Le Teil, and declared at risk of worsening status or even collapsing. The economic loss from the earthquake could reach 50 M€. The Le Teil earthquake corresponds to the most destructive and the strongest earthquake ever felt in France since the Arette (Pyrenees) earthquake in 1967 (M_L 5.3, MSK VII–VIII,)[1,2]. Before this event, the level of instrumental seismicity in the Rhône River Valley was low, and a few damaging historical earthquakes had been documented.

Preliminary seismological analysis indicate a reverse-faulting focal mechanism (FM) along a NE–SW trending fault located within the northeastern termination of the Cévennes Faults system between the Massif Central and the Southeastern basin, with a focal depth between 1 and 3 km (https://www.emsc-csem.org/Earthquake/earthquake.php?id=804595#map). This shallow hypocenter and its proximity to a large limestone quarry raised the question of the possible relationship between the mass of rock extracted and the triggering of the earthquake[3]. This also suggested that the rupture could have reached the surface, which is uncommon for both such a magnitude and for the region.

In this paper, we present the first seismological and geodetical data that helped discover tenuous surface ruptures over a length of about 5 km, and then describe the observations performed in the field. Our study brings new highlights on shallow earthquakes that can occur in stable continental regions, and raises important questions in terms of seismic hazard analyzes, and also in terms of the tectonic processes which are at the origin of this event.

Results

Structural and seismotectonic setting in Le Teil region. The epicenter of the Le Teil earthquake is located at the northeastern part of the Cévennes fault system (CFS) (Fig. 1) in the immediate vicinity of the NE–SW trending La Rouvière fault (LRF)[4]. This fault was not identified as a potentially active fault in the French Active Fault database (BDFA)[5]. Only the two main bounding faults of the CFS, called the Cevennes Fault (CF) and the Marsanne Fault (MF) (see Fig. 1), were considered as potentially active left-lateral strike-slip faults, based on preliminary interpretations of offset geomorphic markers or variations of thickness in quaternary deposits (see ref. [5] and references therein).

The CFS is a major structural boundary between the Massif Central crystalline basement and the sedimentary basin of southeastern France bordering the Alps mountain range, which represents a part of the European continental paleomargin of the Mesozoic Tethys Ocean[6]. The so-called "Ardèche paleomargin" (Fig. 1b) has been extensively studied via seismic reflection profiles, boreholes, gravity modeling, structural modeling, and field observations (e.g. refs. [7–9]). The present-day structure of this region results from several tectonic episodes during which faults

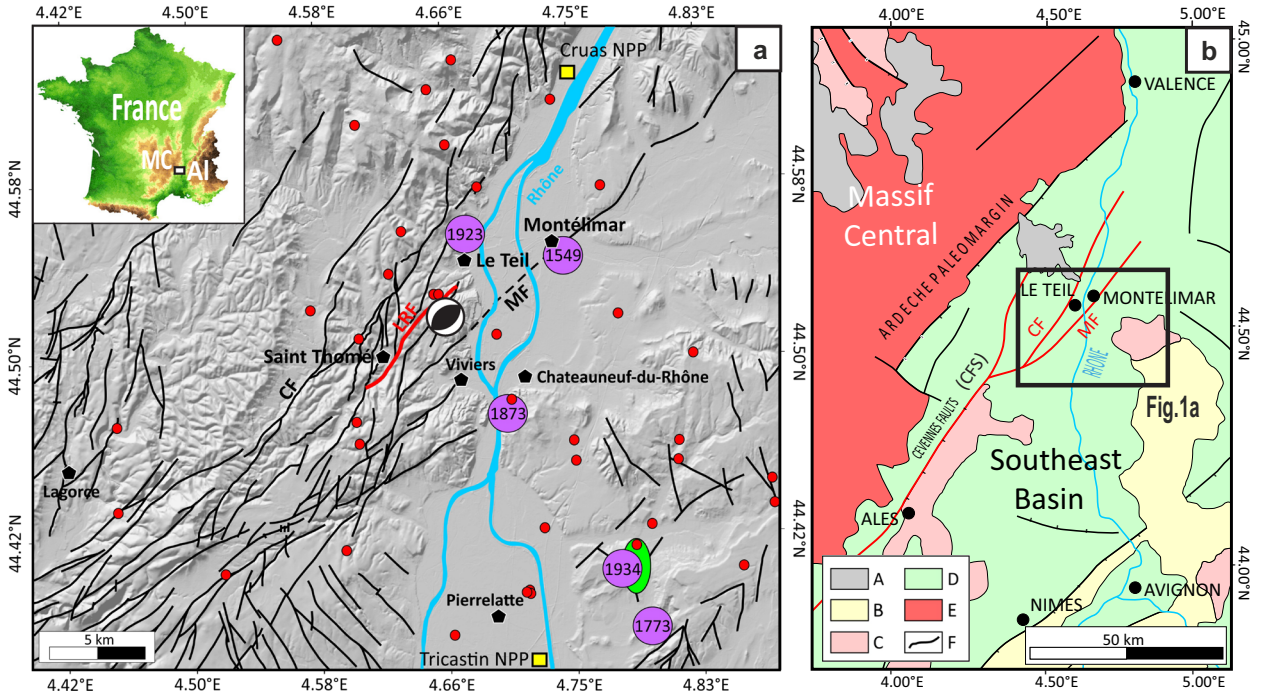

Fig. 1 Structural and seismotectonic setting of the 11 November 2019 Le Teil earthquake. a Seismotectonic map of the Rhône River Valley where occurred the 11 November 2019 M_w 4.9 Le Teil earthquake (44.518°N and 4.671°E). The black and white sphere indicates the reverse-faulting focal mechanism; red and purple circles are instrumental and historical seismicity, respectively; the green ellipse corresponds to the Tricastin swarm; black lines are faults from the Aubenas geological map[4] with the La Rouvière Fault (LRF) in red. CF Cévennes Fault, MF Marsanne Fault. The shaded DTM is from BD ALTI 25 m (IGN); MC and Al in the inset are Massif Central and Alps, respectively. **b** Simplified geological map of the western boundary of the Southeastern Basin (modified from refs. [7,44]). A: Plio-Quaternary volcanism; B: Miocene–Pliocene sediments; C: Oligocene sediments; D: Mesozoic sediments; E: Paleozoic crystalline basement (Massif Central); F: major faults (NE termination of the Cevennes fault system (CFS) in red, CF and MF for Cévennes Fault and Marsanne Fault, respectively). Black dots indicate main population centers.

were reactivated with different kinematics, typical of the Meso-Cenozoic evolution of the western European continental domain[10]. During the early and middle Jurassic, several normal faulting episodes partly reactivated large NE–SW-trending strike-slip structures inherited from the Variscan orogeny, and controlled the development and the deepening of the northern Tethyan margin toward the East[11]. Then, Late Cretaceous to early Eocene N–S-oriented shortening related to the Pyrenean orogenesis led to folding and local reactivation of the CFS as a sinistral strike-slip fault[12]. During Oligocene–early Miocene times, the easternmost segments of the CFS were reactivated as normal faults and accommodated the opening of the Mediterranean Sea[13]. Finally, the easternmost faults of the Ardèche paleomargin have been partly inverted during the late Miocene–Pliocene E–W to NW–SE Alpine compression[7,14]. This complex history led to a structural pattern with ~100-km-long inherited faults, striking NE–SW and dipping to the southeast (Fig. 1). These faults display listric geometries, with some high-angle shallow segments (down to 1–2 km depth), and are rooted at 3–5 km depth in a relatively flat basal detachment into the Carboniferous–Triassic formations or in the early Jurassic strata[7,8].

In situ stress measurements in boreholes and FMs show that the region is located within a NW–SE compressional regime[14,15]. This is confirmed by a recent analysis of geodetic data that also suggests a maximum NW–SE compressional strain rate of $0.7 \times 10^{-9}\,\mathrm{yr}^{-1}$ (ref. [16]).

Seismicity recorded on the ReNaSS [Réseau National de Surveillance Sismique: https://renass.unistra.fr/les-derniers-seismes/page/25] and LDG [Laboratoire de Détection et de Géophysique du Commissariat à l'Energie Atomique: http://www.dase.cea.fr/evenement/evenements.php?type=bulletin&type_bulletin=&identifiant=20191111-105246&lang=fr] seismic networks included 39 earthquakes between 1962 and 2018 within a radius of 20 km around Le Teil village, all having magnitude M_L lower than 2.9 (Fig. 1a). Focal depths for these events are estimated between 5 and 24 km with large uncertainties since the nearest station is located ~30 km away. Potentially several earthquakes could then have been caused by structures in the bedrock, beneath the decollement levels. The distribution of epicenters does not show any particular pattern that could highlight the activity of a given fault, considering their potential dip relative to informed earthquake depths (Fig. 1a). Twenty kilometers southward from Le Teil village, on the eastern bank of the Rhône River, a very shallow seismic swarm (the so-called Tricastin swarm[17]) occurred over several months in 2002–2003 with no corresponding fault at the surface (Fig. 1a). Historical archives report shallow earthquakes (focal depth <5 km) in the same region south of Le Teil[18], with macroseismic intensities up to MSK VII between January and April 1773, between July and August 1873, and in May 1934 (Fig. 1a). An earthquake was located at Le Teil, on 26 November 1923, with I_o IV (MSK) with an equivalent M_w of 3 (ref. [18]). The largest event among these regional historical earthquakes occurred on 8 August 1873, at the end of a 4 months seismic swarm. The epicentral area was located 8 km southward from Le Teil, near Chateauneuf-du-Rhône, and its equivalent moment magnitude was estimated at M_w 4.1 ± 0.4 with a depth of ~3 km[18]. No surface ruptures were reported for these historical earthquakes.

Seismological data—FM. The local magnitude of the 2019 Le Teil earthquake varies from M_L 5.2 (ReNaSS) to M_L 5.45 (LDG). The moment magnitude is M_w 4.9 (this study) and the maximum epicentral intensity is VIII (EMS98) with a wide region (15 km diameter around Le Teil) impacted by at least an intensity VI [BCSF: Bureau central Sismologique Français: http://www.franceseisme.fr/donnees/intensites/detailsseisme.php?IdSei=930]. We benefited from the data of four additional seismological stations located less than 25 km away from the epicenter. Epicentral solutions were mapped by using a non-linear exploration scheme, inverting exclusively the P and S wave arrival times of these four

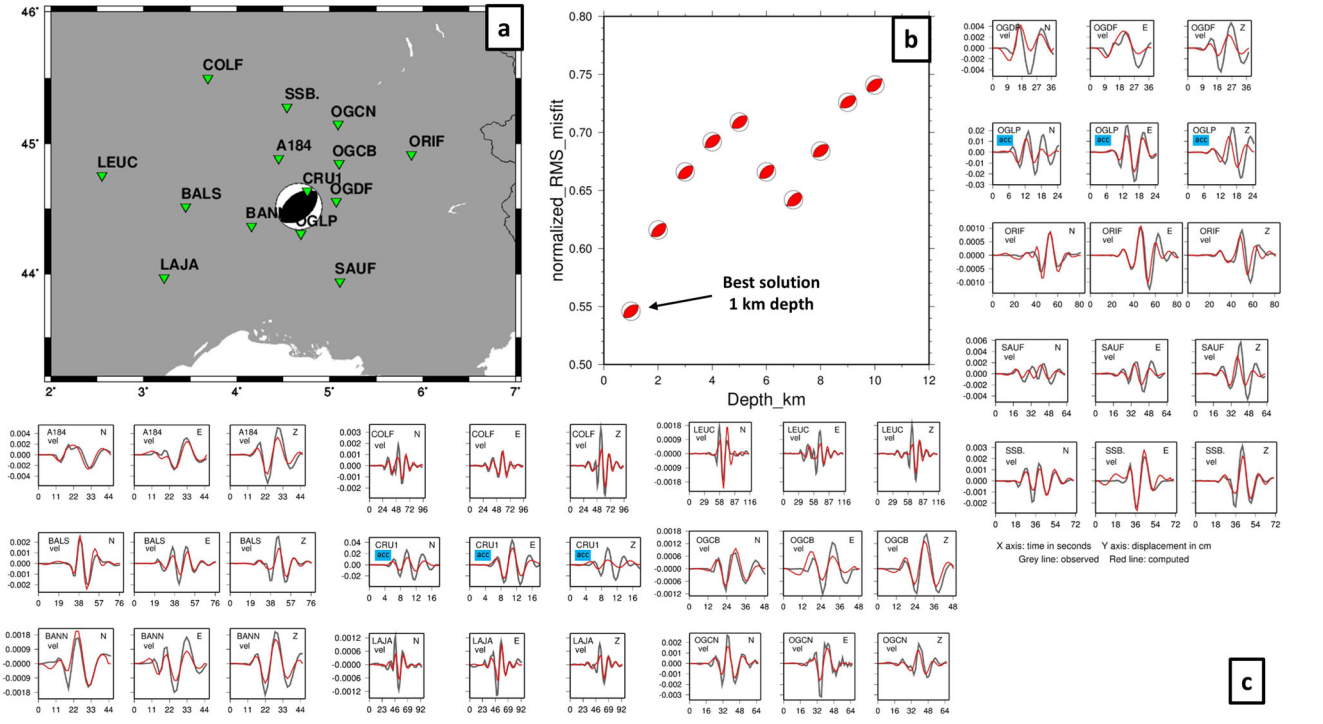

Fig. 2 Result of the waveform inversion. a Map with stations used (green triangles) and the focal mechanism corresponding to the best solution found. **b** Plot of focal mechanism solutions in an RMS versus depth graph. **c** Waveform fit, in displacement (cm) bandpass filtered between 0.03 and 0.08 Hz. Observed records are in gray and computed in red. For each station the three components are displayed (N, E, Z), and "vel" or "acc" (blue labels) means that the original record was in velocity (broadband) or acceleration (strong motion), respectively.

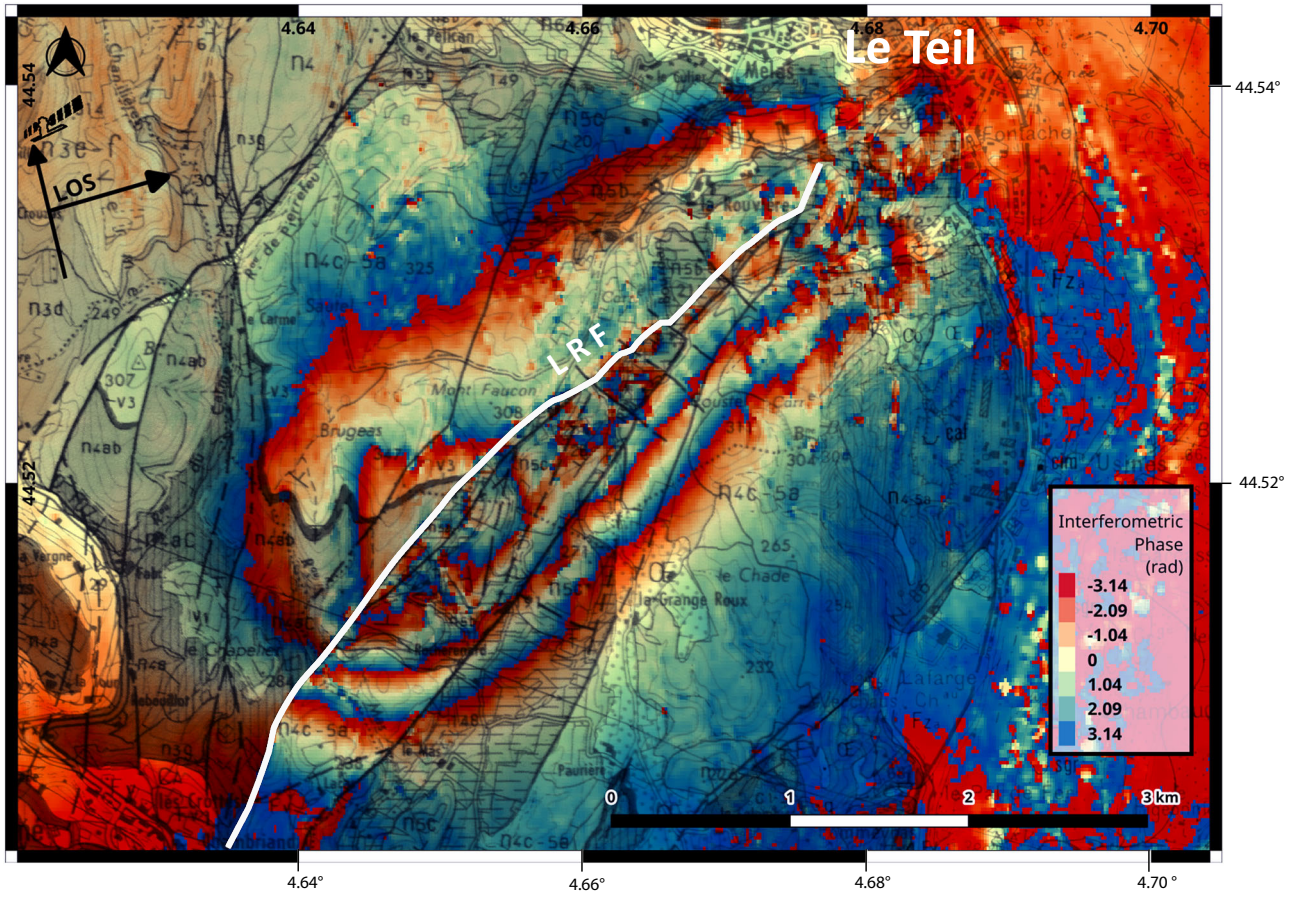

Fig. 3 First interferogram (wrapped phase) obtained using Sentinel-1 synthetic-aperture radar data. Pre-earthquake image is from 31 October 2019; post-earthquake image is from 12 November 2019 (12 days baseline). The black lines correspond to faults after the Aubenas geological map[4]. The white line defines the ~5-km-long northern section of the La Rouvière Fault (LRF) matching with the InSAR discontinuity.

closest stations. In this process, we tested many different 1D velocity models accounting for the uncertainty in the crust properties. Doing so, we could estimate the uncertainty on the absolute location of the epicenter, which resulted to be <1 km.

We determined the double-couple point source FM of the main shock by waveform inversion (FMNEAR method[19]) using the nearest regional unsaturated broadband and strong-motion records (Fig. 2). The inversion has been carried out using a combination of grid search and simulated annealing, allowing an extensive exploration of the parameters space. We selected solutions to minimize the normalized root-mean-square (RMS) misfit function of the waveforms (Fig. 2c). We repeated the inversion for various fixed source depths. In Fig. 2a, only the best solution is shown, but a group of FM solutions has been retrieved with similarly low root-mean-square misfit values, indicating that strike can vary between 45° and 65°, and that the dip angle can vary between 45° and 50°. The best solution corresponds to a strike, dip, and rake of 50°, 45°, and 89°, respectively. Several inversions with different velocity models resulted with 1 km as the best source depth, meaning that the shallow character of the earthquake is a robust characteristic (Fig. 2b). The corresponding moment magnitude is $M_w = 4.9$.

Geodetic data—distribution of the vertical displacement. The surface deformation associated with the Le Teil earthquake was revealed by using synthetic-aperture radar (SAR) images from the Sentinel-1 satellite. We computed a first interferogram with DIAPASON software[20] using a master (pre-seismic) SAR image from 31 October and a post-seismic image from 12 November (12 days baseline) (Fig. 3). This first result showed a very shallow rupture over a length of ~5 km in the NE–SW direction, matching with the northern half of the LRF, an ~10-km-long-fault that runs from Saint-Thomé village to the southwest up to Le Teil village to the northeast (Fig. 1a). The interferogram suggested the uplift of the SE block with respect to the NW one along a southeastern-dipping reverse fault. The number of well-expressed InSAR fringes (5) indicated the expected vertical fault offset might reach ~15 cm.

Using 6-day-baseline master products, we computed two more accurate interferograms using the ESA SNAP Sentinel-1 Toolbox processing software on the Geohazards TEP (Supplementary Table 1 and Notes), from which we extracted the vertical component of co-seismic displacement from the unwrapped interferogram ascending track (Fig. 4a). This allowed us identifying the largest displacement gradient lines, which we interpreted as likely surface breaks. Those gradient lines cross a hilly landscape of Cretaceous terrains dipping gently (~10°) northwestwards with a topography incised by the close Rhône River-related drainage. Elevation decreases eastward from 350 to 50 m (Rhône valley). There are sporadically thin layers of Pliocene to Quaternary soils and deposits (alluvium, colluvium) related to this fluvial history. The displacement gradients are almost entirely located along the inherited LRF between contrasting lithologies (Fig. 4b). We also extracted elevation changes along 14 profiles cross-cutting perpendicularly a projection line following the NE–SW general trend of the gradient lines (see locations on Fig. 4a). Those profiles allowed estimation of the total deformation produced by the earthquake at the surface (Supplementary Data 1,

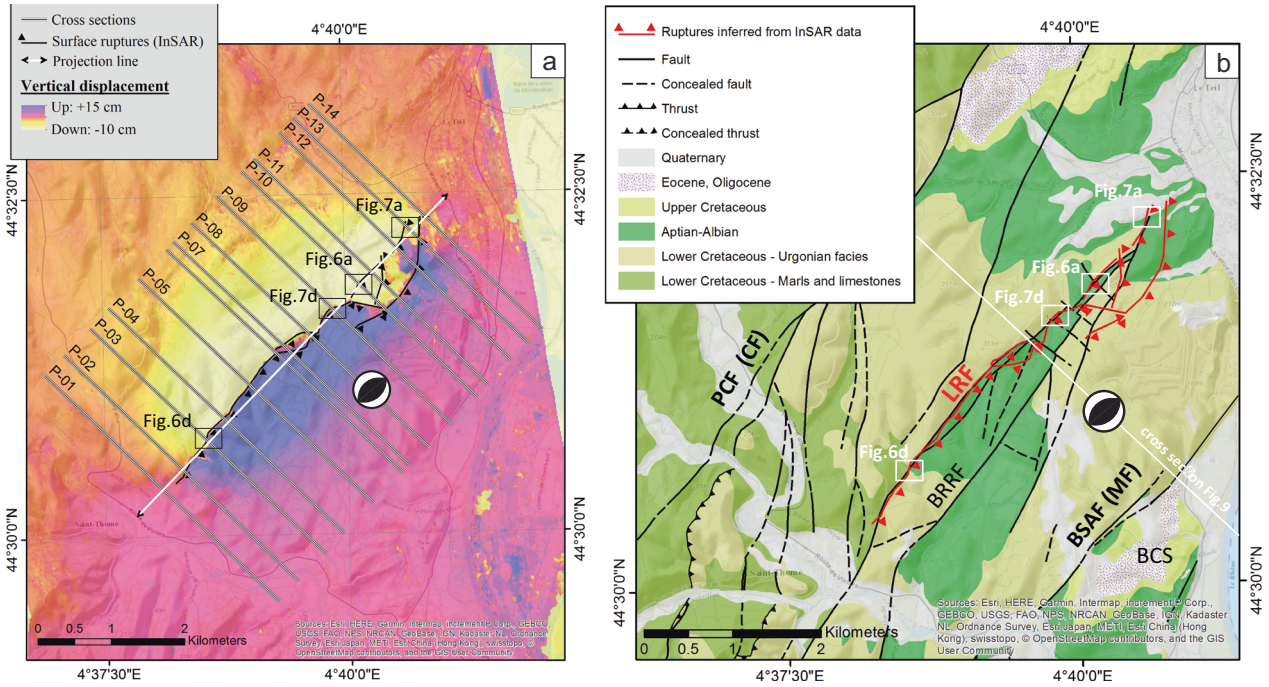

Fig. 4 Map of vertical displacements from InSAR data and map of the main geological formations in the region affected by the Teil earthquake. **a** Vertical displacement associated to the 11 November 2019, M_w 4.9 Le Teil earthquake inferred from the unwrapped InSAR interferogram (ascending track) draped over a satellite image of the area; maximum gradient on this map allows tracing the surface rupture; the epicenter of the event is represented by its focal mechanism; thin black lines correspond to extracted profiles across the rupture to determine the vertical displacement and the width of the deformation zone. **b** Simplified geological map (modified from BRGM) of the Le Teil region highlighting the sharp correspondence between the co-seismic rupture trace inferred from InSAR (in red) and the La Rouvière Fault in black. PCF (CF) Pontet-de-Couloubre Fault (Cevennes Fault), LRF La Rouvière Fault, BRRF Bayne-Roche-Renard Fault, BSAF (MF) Bayne-Saint-Alban Fault (Marsanne Fault), BCS Bayne-Couijanet Syncline.

Supplementary Fig. 1). From the profiles, we reconstructed the distribution of the vertical component of co-seismic slip along the rupture that we compared to the width of the deformation zone (Fig. 5). We observe that the deformation is larger and more localized in the southern part of the rupture, with a principal rupture vertical displacement of 22.5 cm, and a total deformation zone width (TDZW) between 50 and 400 m. In contrast, the northern part displays a wider accommodation zone (TDZW between 400 and 800 m) and lower principal rupture displacements (12–3 cm). A detailed analysis of the profiles shows that the highest gradients are located on the surface trace of the LRF for most of the rupture length (profiles 2–13). Notable exceptions to this trend appear on profiles 10, 11 and 12, where deformation is transferred to unmapped faults to the SE (see Fig. 4).

Based on this analysis, we obtain a "detectable surface rupture length"[21] of 5.16 km. There is no major along-strike change between the lithologies juxtaposed by the fault (Fig. 4b), suggesting that this along-strike evolution of vertical fault displacement vs the accommodation width is mainly controlled by source processes, and likely reflects variations of slip along the fault plane.

Surface rupture observations. We performed field investigations to search for surface rupture within 48 h after the earthquake. The preliminary InSAR analysis (see Fig. 3) was crucial to guide surface rupture investigations as has been demonstrated in similar studies[22–24]. Given the high density of vegetation that covers a large part of the area, we first focused on roads and paths crossing the InSAR discontinuity and found spot evidences of surface rupture. To complement our observations and image the continuity of the rupture below the forest cover, we carried out an airborne LiDAR survey.

The documented surface ruptures generally correspond to open fissures with an NE–SW orientation (see Supplementary Fig. 2, Supplementary Data 2). In a few cases, we observed compressional features such as small folds or reverse faults with the southeastern block systematically thrusting over the northwestern one (Figs. 6 and 7). In total, we observed evidence of surface rupture at 17 separate locations distributed over 4.5 km along the InSAR discontinuity. In order to accurately quantify the subtle deformation of the ground surface, we surveyed the best locations with a terrestrial laser scanner (Faro X330). The measured vertical uplift of the SE compartment is comprised between 2.7 and 13 cm (Figs. 6 and 7), which corresponds to ~45% of the displacement estimated from the InSAR analysis. Overall, this suggests that at surface more than 50% of the deformation is distributed off-fault in a 100–800 m wide zone.

We estimated the equivalent moment magnitude using measured rupture parameters and the equation $M_w = 2/3\log(M_o) - 6.1$ (refs. [25,26]), with $M_o = \mu LWD$, where μ is the shear modulus, L the surface rupture length, W the rupture width at depth, and D the average surface displacement expressed in SI units. We used the following rupture parameters:

- $L = 4600$ (length determined visually from interferograms) to 5200 m (detectable length from the analysis of InSAR profiles).
- $W = 1400$ to 2800 m (considering a focal depth of 1000 ± 500 m, a fault dip of 45°, and assuming that the rupture extended over 500 m in depth from the hypocenter).
- $D = 0.10$ m (mean vertical displacement from Fig. 5) to 0.14 m (accounting for a 45° rupture dip).
- $\mu = 2 \times 10^{10}$ to 2.5×10^{10} Pa, accounting for the shallowness of the rupture and determined from density and shear wave velocities in the stratigraphic layers surrounding the hypocenter (Cornou, personal communication).

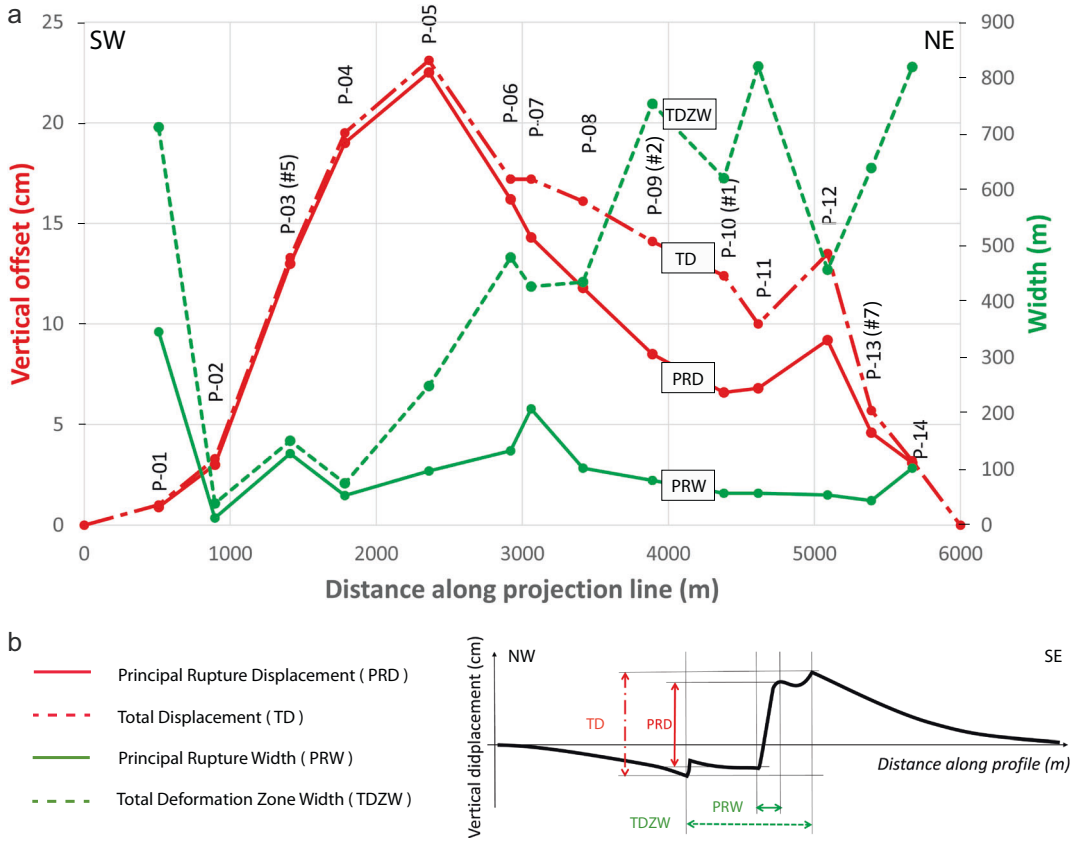

Fig. 5 Distribution of the vertical co-seismic slip and width of the deformation associated with the Le Teil earthquake. a Co-seismic slip distribution and width of the deformation zone inferred from InSAR data, along the projection line indicated in Fig. 4a. This graph is based on 14 across fault profiles that were traced at key locations where we observed deformation features in the field. Those profiles allow the estimation of vertical displacement across the rupture (vertical offset), together with the width across which this displacement is accommodated. As shown in **b**, we distinguish two levels of observation aperture along each profile: the total deformation zone (TD and TDZW) that describes the whole deformation band, and the principal rupture (PRD and PRW) where most of the vertical offset is concentrated with the highest gradient. See Supplementary Notes for more information.

This yields a geological equivalent moment magnitude M_w between 4.7 and 5.0, which is consistent with the moment magnitude estimated from the seismological data.

Figure 8 shows the location of the 17 surface rupture observations plotted on a 25-cm-resolution bare-earth digital elevation model (DEM) obtained from a lidar survey that we carried out 10 days after the earthquake. A detailed analysis of the point cloud did not yield new evidence of surface rupture to complement field data. We interpret this as the combination of small offsets, dense vegetation cover (and conversely sparse ground data points), soft forest soil that distributes the deformation and intense rainfall between the time of the earthquake and the time of the Lidar survey. Overall, we can observe that 10 observations—among which the four main evidences numbered 1, 2, 5, and 7 shown in Figs. 6 and 7—are located upon the inherited Oligocene normal fault LRF, which defines a clear and continuous topographic scarp in the DEM.

Relationships between the rupture and the ancient LRF Fault. In the field, the fault scarp associated with the LRF exhibits several normal fault planes in competent lower Cretaceous (Barremian) carbonates exhumed by agricultural land use and/or differential erosion where carbonates are juxtaposed to marl-rich units (Fig. 4b). These fault planes strike mainly N30–40°E and dip between 45 and 60°E, with steep slickenlines indicating in a few places an unambiguous normal cumulative movement with a slight left-lateral component. As already pointed out from the InSAR analysis, these observations show that the Le Teil earthquake rupture occurred along the ancient Oligocene normal LRF, but with reverse-faulting kinematics. Moreover, we could not find yet, in the field or after the DEM analysis, any clear evidence of previous cumulative reverse-faulting activity prior to Le Teil event such as recent reverse-fault scarps, even diffuse. The morphology of the LRF fault zone, when it is preserved from anthropogenic activity, corresponds to that of an ancient cumulative normal fault scarp that has undergone differential erosion through time.

In order to analyze the relationship between reverse-faulting during the 11 November 2019 earthquake and the Oligocene inherited normal faults located in the epicentral area, we performed a geological cross-section along the InSAR-derived vertical displacement profile no. 8 (see Fig. 4 for location and Supplementary Notes), that encompasses the earthquake epicenter (Fig. 9). The different faults of the northern CFS correspond to ancient listric normal faults as observed along a seismic profile 20 km further to the southwest[8]. This listric geometry is consistent with the slight northwestwards tilt of the Mesozoic units (~10° NW). The depth of the earthquake (1.0 ± 0.5 km) suggests that the rupture initiated below, or at the boundary with, the shallow massive Barremian limestones (~700-m-thick), within the Valanginian marls and limestones unit (~1700-m-thick). The earthquake hypocenter aligns with the projection of the surface trace of the LRF at depth considering a dip range of 45–60°SE. This strongly suggests that the 11 November 2019 Le Teil earthquake nucleated on the LRF at depth, which is consistent with our analyses of the InSAR and surface rupture observations

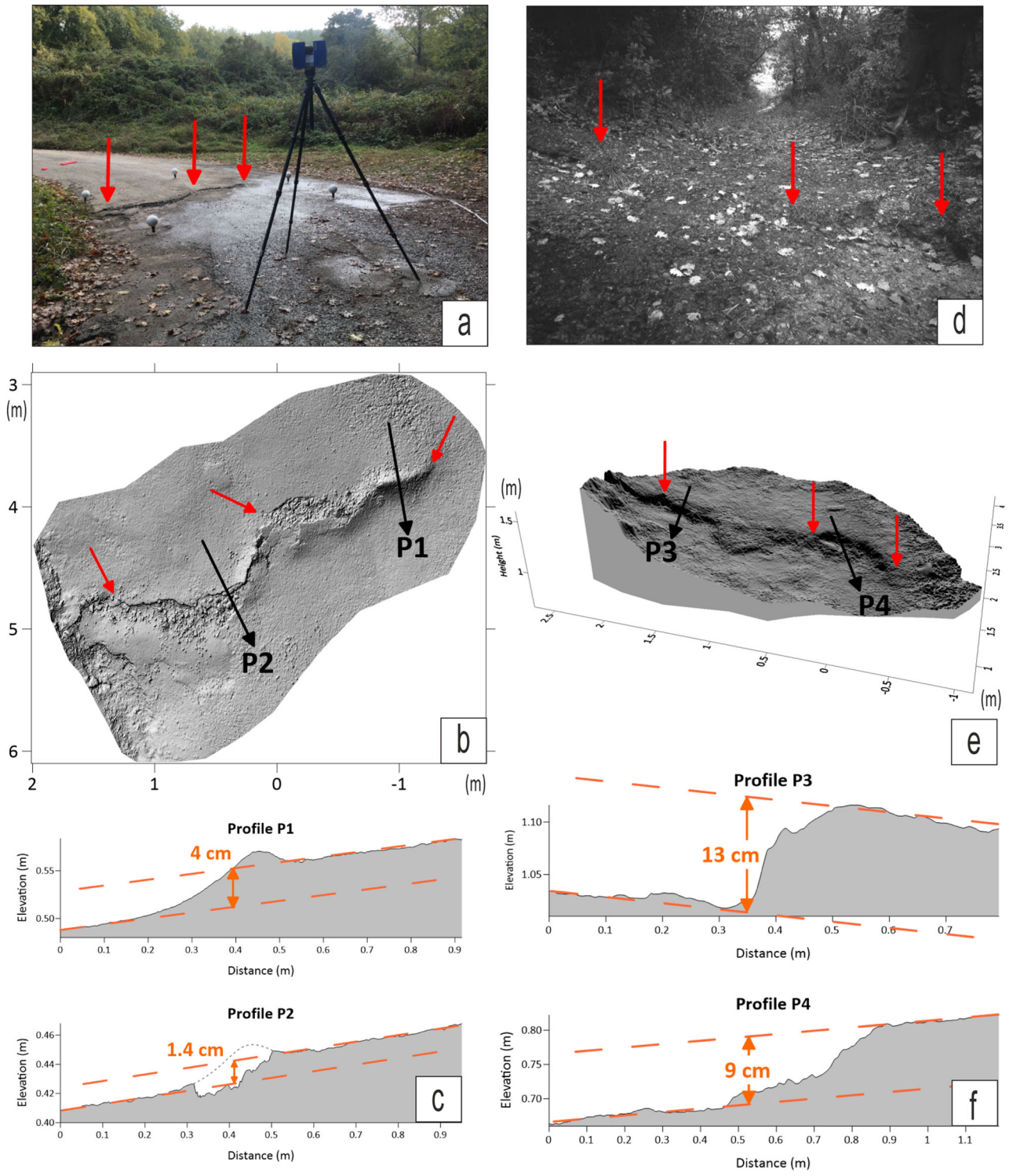

Fig. 6 Examples of surface ruptures and associated deformation measurements. a, **d** Field photographs showing surface ruptures affecting an asphalt road and a dirt path (evidences #1 and #5, respectively, see location Fig. 4). Red arrows point to the rupture. Equipment visible in **a** is a laser scanner used in the following. **b**, **e** Ultra-high-resolution (1 mm) laser scans at the same locations. Red arrows point to the same locations as in field photographs. **c**, **f** Topographic profiles extracted from laser scans, showing the vertical components.

showing that the co-seismic deformation is localized with the geological surface trace of the LRF.

Discussion

Our observations show that the very shallow M_w 4.9 Le Teil earthquake is associated with the reactivation of the LRF, an ancient fault belonging to the CFS characterized by a strong tectonic inheritance. One of the peculiarities of the event is its remarkable surface rupture. At the worldwide scale, such a low-magnitude event has a low probability (<10%) of rupturing the surface[27], but the extreme shallowness of the Le Teil event explains its occurrence. Similar events have been described in

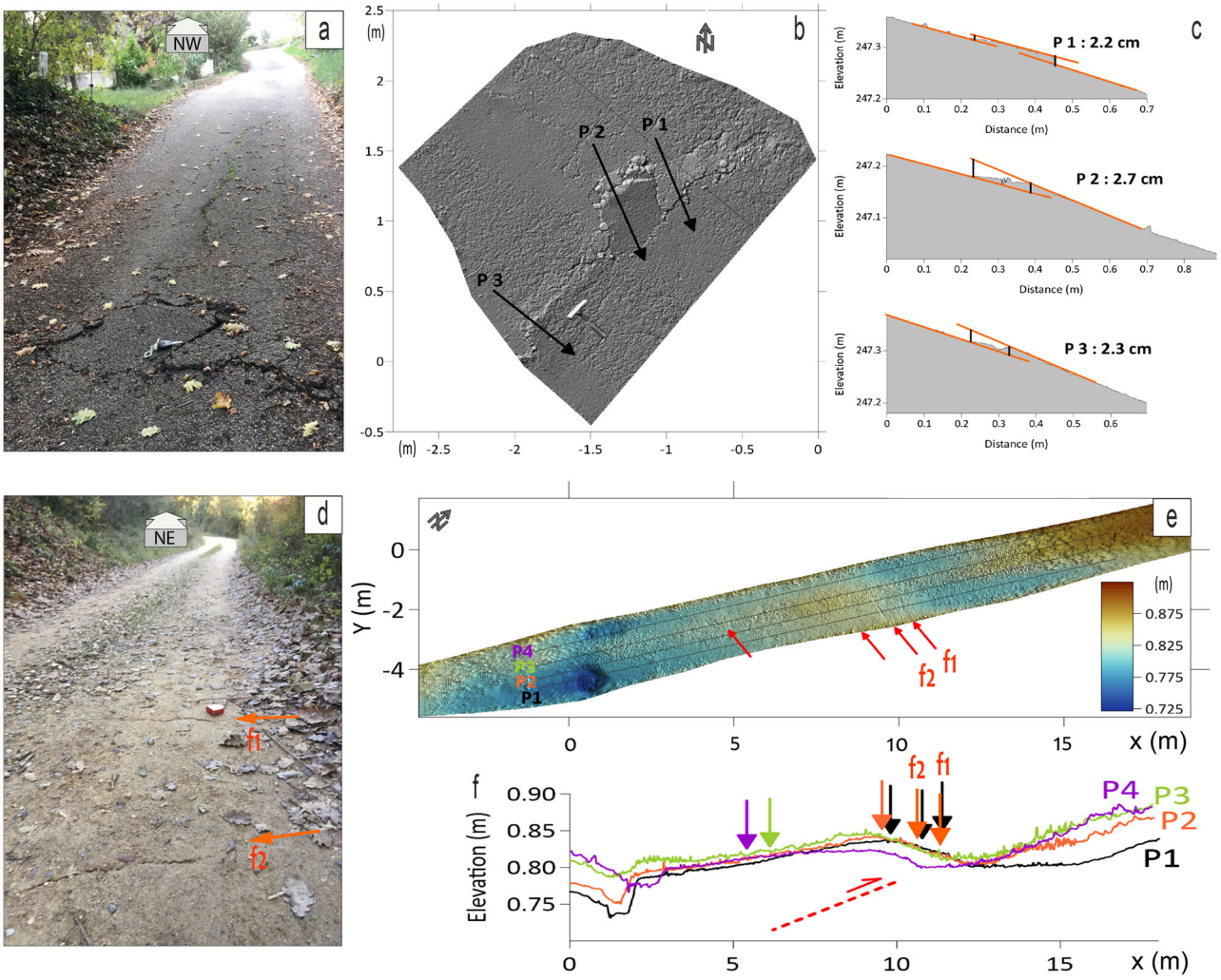

Fig. 7 Examples of surface ruptures and associated deformation measurements. a, **d** Field photographs showing surface ruptures affecting an asphalt road (flat pop-up structure) and a dirt road (extrados-fissures) (evidences # 7 and # 2, respectively, see location Fig. 4). **b**, **e** Ultra-high-resolution (1 mm) laser scans at the same locations. Blacks arrows in **b** correspond to profiles shown in **c**; red arrows in **e** points to N090–N100°E trending fissures (the two northeastern are those shown in **d**). The thin black lines correspond to the four topographic profiles shown in **f**. Note the position of cracks on top of what we interpreted as a 5 m long bulge affecting the dirt road. **c**, **f** Topographic profiles extracted from laser scans, showing the vertical components (the red dotted line in **f** corresponds to the suspected reverse-fault rupture controlling the bulge of the dirt road).

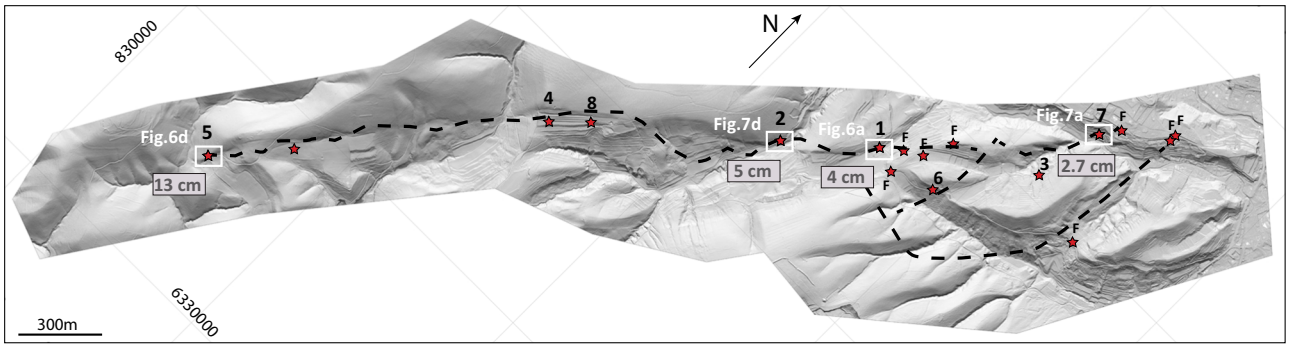

Fig. 8 Location of surface rupture observations (red stars) on a 25-cm-resolution shaded relief topographic map of the LRF fault scarp. The DEM is obtained from a post-earthquake airborne lidar survey (UTM grid). Numbers refer to main evidence described in the text (see Figs. 6 and 7 and Supplementary Figs. 2 and 3; vertical offset in rectangles), while "F" refers to open fissures affecting asphalt roads.

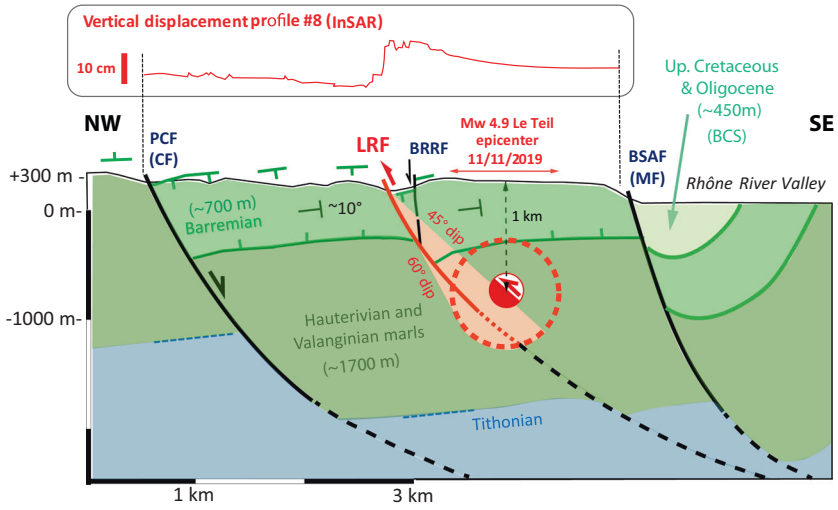

Fig. 9 Geological cross-section showing the possible relationship between the Oligocene inherited normal La Rouvière fault (LRF) and the reverse 11/11/2019 earthquake rupture (red). Thickness, dip, and location of geological formations are from the Aubenas geological map[4]. Elevation is from Google Earth extraction. PCF Pontet-de-Couloubre Fault, LRF La Rouvière Fault, BRRF Bayne-Roche-Renard Fault, BSAF Bayne-Saint-Alban Fault, BCS Bayne-Couijanet Syncline.

normal and strike-slip environments as well, for instance in Peru (1986 M_w 5.2 Cusco[28]), in Ecuador (2010 M_w 4.9 Pisayambo[23]), in the western French Alps (1995 ML 5.3 Epagny[29]), or in Grece (2011 M_w 4.8 Siamo[30]), respectively. Furthermore, noticeable earthquake ruptures with reverse mechanisms broke the surface in very active (e.g. 1983 M 4.5 Nunez, California) or stable continental regions like Australia with the 1970 M_w 5 Calingiri and 2007 Mw 4.7 Kataning earthquakes[24,31].

The LRF was not previously identified as potentially active[5] given that it does not display noticeable instrumental seismicity or geomorphologic expression that would suggest measurable tectonic activity since the Oligocene. Differential erosion of geological formations and structures as well as human activity (i.e. numerous agricultural terraces) favor the expression of the NE–SW structural fabric associated with the Oligocene extension as the main geomorphological pattern in the landscape. The absence of geomorphologic evidence for reverse faulting before the Le Teil earthquake along the LRF pointed out during our preliminary observations suggests that the fault has not broken for a long time (i.e. several thousand or even tens of thousands of years). This may be due to the very low NW-SE maximum compressional strain rate for the region (i.e. $0.7 \times 10^{-9}\,\mathrm{yr}^{-1}$ (ref. [16])), and the likely very long associated earthquake recurrence intervals during which evidences of surface deformation may be erased from the landscape. If this low strain rate is distributed regionally across different segments of the CFS (Figs. 1 and 4b), such effect would be amplified. In such conditions, the preservation of geomorphological markers such as tenuous fault scarps seems improbable, especially considering the millennial-scale denudation rates obtained for the Massif Central region (i.e. between 40 and 80 m/Ma[32]).

Our observations and inferences raise several important questions for seismic hazard analyses in stable continental regions. The first of these questions is to ask whether faults or fault segments composing the northern CFS (including LRF) have broken in the recent past, and what are their seismogenic potential? Deep geophysical imaging surveys should assess the crustal nature of these structures, their dimensions and potential to produce M_w 6+ earthquakes while paleoseismological studies should help defining the timing of such events. These upcoming studies will hopefully allow improving the existing fault model used in site-specific (e.g. ref. [33]) or regional scale (e.g. ref. [34]) Probabilistic Seismic Hazard analyses, by specifying earthquake recurrence (if any), slip rates, and inferring expected large magnitudes.

Increasingly, surface rupture hazard is considered a significant threat for widespread lifelines, infrastructures, and critical facilities. In France and surrounding intraplate areas, this hazard is rarely taken into account although it exists, as the Le Teil earthquake case strikingly shows. To date, this hazard is essentially analyzed based on empirical approaches to anticipate the location and amplitude of localized slip along the surface trace of an active fault. Avoidance zones can be defined around the expected earthquake fault (e.g. refs. [35,36]). All those empirical approaches suffer the scarcity of datasets, in the low-to-moderate magnitude range of events, rendering poorly constrained hazard assessment. This issue is being addressed by an international initiative of data collection[37] that will be enhanced by Le Teil case study.

There are also questions regarding the NW–SE compression invoked as the "long term" (i.e. several 100 ka) tectonic process responsible for the earthquake. The epicentral region is characterized by low strain rates (e.g. refs. [16,38]), and tectonic loading as the main driving mechanism for seismicity has recently been questioned for such regions (e.g. ref. [39]), putting forward the possible one-off character of such earthquakes (such as in Australia[24]). Genti et al.[40] suggest that the present local stress field could be related to the uplift of the Massif Central and the Alps induced by erosional and/or post-glacial rebound processes (see also refs. [41–43]). Addressing those geodynamic issues will mobilize a series of large-scale geological and geophysical data and modeling approaches, well beyond the scope of this paper.

In conclusion, the 11 November 2019 M_w 4.9 Le Teil earthquake is a historically unprecedented earthquake in France and surrounding region. Firstly, because it displays very low magnitude and shallow surface-rupturing characteristics, and secondly because comprehensive seismological, geodetical, and surface rupture observations could be performed with modern techniques. For those reasons, the Le Teil earthquake represents a unique opportunity and a turning point to better define the

seismicity to consider for hazard studies. Indeed, the risk of surface-rupturing events in France or similar stable continental regions is until now considered to be negligible in most regions due to the very low strain rate measurements.

Methods

The different methods we used in this work are integrated into the description of the results and detailed in the Supplementary Information files.

Data availability

InSAR Sentinel data are accessible on the ESA website: https://scihub.copernicus.eu/dhus. The seismological data used and analyzed during the current study are available at: https://doi.org/10.15778/RESIF.FR, https://doi.org/10.15778/RESIF.RA, https://doi.org/10.18715/GEOSCOPE.G, https://doi.org/10.12686/alparray/z3_2015. The terrestrial laser scans of surface deformation (Data set) associated with the 11/11/2019 M_w 4.7 Le Teil earthquake (SE France) at https://zenodo.org/record/3928606#.Xv7j7-dBpaQ. Geological (surface ruptures evidences) and InSAR data generated or analyzed during this study are included in this published article (and its Supplementary Information files).

Received: 14 February 2020; Accepted: 3 July 2020;
Published online: 27 August 2020

References

1. Gagnepain, J. et al. Sismicité de la region d'Arette (P.A.) et mécanismes au foyer. *Ann. Geophys.* **36**, 499–508 (1980).
2. Cara, M., Alasset, P. J. & Sira, C. in *Historical Seismology, Modern Approaches in Solid Earth Sciences* (eds. Fréchet, J. et al.) Vol. 2, 363–378 (Springer, Dordrecht, 2008).
3. Ampuero, J. P. et al. The November 11 2019 Le Teil, France M5 earthquake: a triggered event in nuclear country. EGU General Assembly, 4–8 May 2020 (2020).
4. Elmi, S. et al. Notice 53 explicative, Carte géologique de France (1/50 000), Feuille Aubenas (865), Orléans: BRGM, 170 p. 54. Carte géologique par Y. Kerrien (coord.), S. Elmi, R. Busnardo, G. Camus, G. Kieffer, J. Moinereau, 55 A. Weisbrod (1989) (1996).
5. Jomard, H. et al. Transposing an active fault database into a seismic hazard fault model for nuclear facilities—Part 1: Building a database of potentially active faults (BDFA) for metropolitan France. *Nat. Hazards Earth Syst. Sci.* **17**, 1573–1584 (2017).
6. Crunelle, R. & Dubois, P. Evolution mésozoïque des grands bassins sédimentaires Français (Bassin de Paris, d'Aquitaine et du Sud-Est). *Bull. Soc. Géol. France, II* **4**, 529–546 (1986).
7. Roure, F., Brun, J. P., Colletta, B. & Van den Driessche, J. Geometry and kinematics of extensional structures in the Alpine Foreland Basin of southeastern France. *J. Struct. Geol.* **14**, 503–519 (1992).
8. Roure, F., Brun, J. P., Colletta, B. & Vially, R. in *Hydrocarbon and Petroleum Geology of France*, Special Publication of the European Association of Petroleum Geoscientists (ed. Mascle, A.) Vol. 4, 245–268, (Springer, Berlin, Heidelberg, 1994).
9. Bonjoly, D. et al. the GPF team, The Ardèche paleomargin of the Sout-East Basin of France: Mesozoic evolution of a part of the Tethyan continental margin (Géologie Profonde de la France programme). *Mar. Petrol. Geol.* **13**, 607–623 (1996).
10. De Graciansky, P. C., Dardeau, G., Lemoine, M. & Tricart, P. *The inverted margin of the French Alps and foreland basin inversion*. Inversion Tectonics (eds Cooper, M. A. & Williams, G. D.) Vol. 44, 87–104 (Geological Society, London, 1989).
11. Dercourt, J. et al. Geological evolution of the Tethys belt from Atlantic to Pamirs since the Lias. *Tectonophysics* **123**, 241–315 (1986).
12. Arthaud, F. & Séguret, M. Les structures pyrénéennes du Languedoc et du Golfe du Lion (Sud de la France). *Bull. Soc. Géol. France* **4**, 51–63 (1981).
13. Séranne, M. *The Gulf of Lion continental margin (NW Mediterranean) revisited by IBS: An overview*. The Mediterranean Basins: Tertiary Extension within the Alpine Orogen (eds Durand, B., Jolivet, L., Horvath, F. & Séranne, M.) Vol. 156, 15–36 (Geological Society, London, 1999).
14. Blès, J. L. & Gros, Y. Stress field changes in the Rhone Valley from the Miocene to the present. *Tectonophysics* **194**, 265–277 (1991).
15. Rebaï, S., Philip, H. & Taboada, A. Modern tectonic stress field in the Mediterranean region: evidence for variation in stress directions at different scales. *Geophys. J. Int.* **110**, 106–140 (1992).
16. Masson, C., Mazzotti, S., Vernant, P. & Doerflinger, E. Extracting small deformation beyond individual station precision from dense Global Navigation Satellite System (GNSS) networks in France and western Europe. *Solid Earth* **10**, 1905–1920 (2019).
17. Thouvenot, F., Jenatton, L. & Gratier, J. P. 200-m-deep earthquake swarm in Tricastin (lower Rhône Valley, France) accounts for noisy seismicity over past centuries. *Terra Nova* **21**, 203–201 (2009).
18. Manchuel, K. et al. The French seismic CATalogue (FCAT-17). *Bull. Earthquake Eng.* **16**, 2227–2251 (2018).
19. Delouis, B. FMNEAR: determination of focal mechanism and first estimate of rupture directivity using near-source records and a linear distribution of point sources. *Bull. Seismol. Soc. Am.* **104**, 1479–1500 (2014).
20. Massonnet, D. Satellite radar interferometry. *Sci. Am.* **276**, 46–53 (1997).
21. Clark, D. J. et al. Surface deformation relating to the 2018 Lake Muir earthquake sequence, southwest Western Australia: new insight into stable continental region earthquakes. *Solid Earth* **11**, 691–717 (2020).
22. DeLong, S. B. et al. Tearing the terroir: details and implications of surface rupture and deformation from the 24 August 2014 M6.0 South Napa earthquake, California. *Earth Space Sci.* **3**, 416–430 (2016).
23. Champenois, J. et al. Evidences of surface rupture associated with a low-magnitude (Mw 5.0) shallow earthquake in the Ecuadorian Andes: Andean earthquake surface rupture. *J. Geophys. Res. Solid Earth* **122**, 8446–8458 (2017).
24. King, T., Quigley, M. & Clark, D. Surface-rupturing historical earthquakes in Australia and their environmental effects: new insights from re-analyses of observational data. *Geosciences* **9**, 408 (2019).
25. Kanamori, H. The energy release in great earthquake. *J. Geophys. Res.* **82**, 2981–2987 (1977).
26. Hanks, T. & Kanamori, H. A moment magnitude scale. *J. Geophys. Res.* **84**, B5 (1979).
27. Moss, R. E. S. & Ross, Z. E. Probabilistic fault displacement hazard analysis for reverse faults. *Bull. Seismol. Soc. Am.* **101**, 1542–1553 (2011).
28. Cabrera, J. & Sébrier, M. Surface rupture associated with a 5.3-mb earthquake: the 5 April 1986 Cuzco earthquake and kinematics of the Chincheros-Quoricocha faults of the High Andes, Peru. *Bull. Seismol. Soc. Am.* **88**, 242–255 (1998).
29. Thouvenot, F. et al. The Ml 5.3 Epagny (French Alps) earthquake of 1996 July 15: a long awaited event on the Vuache fault. *Geophys. J. Int.* **135**, 876–892 (1998).
30. Kyriakopoulos, C. et al. Monthly migration of a tectonic seismic swarm detected by DInSAR: Southwest Peloponnese, Greece. *Geophys. J. Int.* **194**, 1302–1309 (2013).
31. Dawson, J., Cummins, P., Tregoning, P. & Leonard, M. Shallow intraplate earthquakes in Western Australia observed by Interferometric Synthetic Aperture Radar John. *J. Geophys. Res.* **113**, B11408 (2008).
32. Olivetti, V., Godard, V. & Bellier, O., ASTER Team. Cenozoic rejuvenation events of Massif Central topography (France): insights from cosmogenic denudation rates and river profiles. *Earth Planet. Sci. Lett.* **444**, 179–191 (2016).
33. Clément, C., Scotti, O., Bonilla, L. F., Baize, S. & Beauval, C. Zoning versus faulting models in PSHA for moderate seismicity regions: preliminary results for the Tricastin nuclear site, France. *Boll. Geofis. Teor. E Appl* **45**, 187–204 (2004).
34. Marin, S., Avouac, J. P., Nicolas, M. & Schlupp, A. A probabilistic approach to seismic hazard in metropolitan France. *Bull. Seismol. Soc. Am.* **94**, 2137–2163 (2004).
35. Boncio, P., Liberi, F., Caldarella, M. & Nurminen, F.-C. Width of surface rupture zone for thrust earthquakes: implications for earthquake fault zoning. *Nat. Hazards Earth Syst. Sci.* **18**, 241–256 (2018).
36. Petersen, M. D. et al. Fault displacement hazard for strike-slip faults. *Bull. Seismol. Soc. Am.* **101**, 805–825 (2011).
37. Baize, S. et al. A worldwide and unified database of surface ruptures (sure) for fault displacement hazard analyses. *Seismol. Res. Lett.* **91**, 499–520 (2020).
38. Nocquet, J. M. & Calais, E. Crustal velocity field of Western Europe from permanent GPS array solutions, 1996-2001. *Geophys. J. Int.* **154**, 72–88 (2003).
39. Calais, E., Camelbeeck, T., Stein, S., Liu, M. & Craig, T. J. A new paradigm for large earthquakes in stable continental plate interiors. *Geophys. Res. Lett.* **43**, https://doi.org/10.1002/2016GL070815 (2016).
40. Genti, M., Chery, J., Vernant, P. & Rigo, A. Impact of gravity forces and topography denudation on normal faulting in Central–Western Pyrenees: insights from 2D numerical models. *C. R. Geosci.* **348**, 173–183 (2016).
41. Vernant, P. et al. Erosion-induced isostatic rebound triggers extension in low convergent mountain ranges. *Geology* **41**, 467–470 (2013).
42. Nocquet, J. et al. Present-day uplift of the western Alps. *Sci. Rep.* **6**, 28404 (2016).
43. Malcles, O. et al. Determining the Plio-Quaternary uplift of the southern French Massif-Central; a new insights for intraplate orogen dynamics. *Solid Earth Discuss.* https://doi.org/10.5194/se-2019-99 (2020).
44. Chantraine, J., Autran, A. & Cavelier, C. *Carte géologique de la France*, 6ème édn, 1:1000000 (BRGM, Orléans, 1996).

Acknowledgements

This work was supported by the INSU-CNRS, the "Failles actives France" program (FACT) of the Transverse Seismicity Action (ATS) of the French Seismologic and Geodetic Network RESIF, the Institute of Radiological Protection and Nuclear Safety (IRSN), the Terradue company, and the following research laboratories: Geosciences Montpellier, ISTerre Grenoble, and Geoazur. Sentinel-1 satellite data were freely provided within the framework of the European Commission COPERNICUS program. We thank IRSN and EDF for making available the data of their seismologic stations. We are grateful to the Ronjon, Clauzel, Theron, Vincent, and Quartier families for allowing us to work on their lands. We thank P. Arroucau, J. Billant, A. Combey, C. Cornou, M. Cushing, E. Hannouz, P-H. Leloup, K. Manchuel, and C. Sue for fruitful discussions.

Author contributions

J.-F.R. led field investigations, contributed to collecting and analyzing field data, synthetizing results, and writing the manuscript. S.B. contributed to collecting and analyzing field data, analyzing InSAR data, synthetizing the seismotectonic framework, and writing the manuscript. M.F. contributed to collecting and analyzing field data, analyzing terrestrial laser scanner and LiDAR data, and writing the manuscript. C.L. contributed to collecting and analyzing field data, synthetizing the seismotectonic framework, and writing the manuscript. L.A. contributed to collecting and analyzing field data, analyzing LiDAR data, and writing the manuscript. B.D. contributed to collecting and analyzing seismological data, and writing the manuscript. E.M. contributed to analyzing InSAR data.

Competing interests

The authors declare no competing interests.

Additional information

Supplementary information is available for this paper at https://doi.org/10.1038/s43247-020-0012-z.

Correspondence and requests for materials should be addressed to J.-F.R.

Peer review information Primary handling editor: Joe Aslin.

Reprints and permission information is available at http://www.nature.com/reprints

Publisher's note Springer Nature remains neutral with regard to jurisdictional claims in published maps and institutional affiliations.